metals

MDPI

Article

Influence of Hot Rolling on Microstructure, Corrosion and Mechanical Properties of Mg–Zn–Mn–Ca Alloy

Stanislav O. Rogachev [1,2,*], Viacheslav E. Bazhenov [3], Vasiliy A. Bautin [4], Anna V. Li [1], Sofia V. Plegunova [5], Denis V. Ten [1], Viacheslav V. Yushchuk [1], Alexander A. Komissarov [1,6] and Kwang Seon Shin [6,7]

1 Department of Physical Metallurgy and Physics of Strength, National University of Science and Technology MISIS, 119049 Moscow, Russia; anna23-95@mail.ru (A.V.L.); teden92@yandex.ru (D.V.T.); slava_yushchuk@mail.ru (V.V.Y.); komissarov@misis.ru (A.A.K.)
2 Baikov Institute of Metallurgy and Materials Science, Russian Academy of Sciences, 119334 Moscow, Russia
3 Casting Department, National University of Science and Technology MISIS, 119049 Moscow, Russia; v.e.bazhenov@misis.ru
4 Department of Metallurgy Steel, New Production Technologies and Protection of Metals, National University of Science and Technology MISIS, 119049 Moscow, Russia; bautin@list.ru
5 Laboratory of Biomedical Nanomaterials, National University of Science and Technology MISIS, 119049 Moscow, Russia; plegunova.sv@misis.ru
6 Laboratory of Medical Bioresorption and Bioresistance, Russian University of Medicine, 127473 Moscow, Russia; ksshin@snu.ac.kr
7 Magnesium Technology Innovation Center, Department of Materials Science and Engineering, Seoul National University, 1 Gwanak-ro, Gwanak-gu, Seoul 08826, Republic of Korea
* Correspondence: csaap@mail.ru; Tel.: +7-903-967-5782

Abstract: The effect of hot rolling on the microstructure, mechanical, and corrosion properties of the magnesium alloy 96 wt% Mg–2.3 wt% Zn–0.7 wt% Ca–1 wt% Mn was studied. After heat treatment, the original plates of an as-cast alloy were rolled from a 7 mm thickness to a 0.2 mm thickness at two temperatures—300 or 400 °C. It has been established that increasing the rolling temperature from 300 to 400 °C increases the fraction of recrystallized grains in the microstructure and after rolling at 400 °C, the microstructure is fully recrystallized. The best strength–ductility balance of the alloy was obtained after rolling at 300 °C, with a high total percentage reduction of 93–97%: the yield stress, the ultimate tensile strength, and the elongation averaged at 285 MPa, 310 MPa, and 5%, respectively. The alloy after rolling, annealed at 400 °C, shows improved ductility but lower strength: the yield stress, the ultimate tensile strength, and the elongation were 200 MPa, 260 MPa, and 17%, respectively. The strong dependence of corrosion resistance on respect to rolling direction is observed, which can be reduced after heat treatment. The as-rolled alloy and the heat-treated alloy had low corrosion rates in Hanks' solution of 0.54 and 0.19 mm/year, respectively.

Keywords: Mg–Zn–Mn–Ca alloy; hot rolling; microstructure; strength; plasticity; corrosion resistance

Citation: Rogachev, S.O.; Bazhenov, V.E.; Bautin, V.A.; Li, A.V.; Plegunova, S.V.; Ten, D.V.; Yushchuk, V.V.; Komissarov, A.A.; Shin, K.S. Influence of Hot Rolling on Microstructure, Corrosion and Mechanical Properties of Mg–Zn–Mn–Ca Alloy. *Metals* **2024**, *14*, 1249. https://doi.org/10.3390/met14111249

Academic Editor: Changdong Gu

Received: 11 September 2024
Revised: 17 October 2024
Accepted: 29 October 2024
Published: 4 November 2024

1. Introduction

Biodegradable magnesium-based alloys are used as load-bearing orthopedic temporary implants [1–4]. There are several magnesium alloying systems that have excellent corrosion characteristics, including Mg–Zn–Ga–Y and Mg–Y–Zn–Mn [5–12]. Among the magnesium-based alloys used for medical applications, the Mg–Zn–Ca–Mn system has been widely studied, since all the constituent chemical elements (Mg, Zn, Ca, and Mn) are present in human tissues as nutritional elements [13–16]. In addition, manganese effectively refines grains in Mg–Zn–Ca alloys and, consequently, improves their mechanical properties [17–21], as well as their corrosion properties [15,21]. These alloys demonstrate a low cytotoxicity grade (0–1) according to ISO 10993-5:1999 [13,22,23]. At the same time, Mg–Zn–Ca–Mn as-cast alloys have poor mechanical properties [17,22]. Improving the strength and ductility of these alloys is possible using conventional deformation methods, such as hot

rolling or hot extrusion and severe plastic deformation; for example, equal-channel angular extrusion [13,24–28]. Bazhenov et al. studied a promising alloy for orthopedic implants, namely 96 wt% Mg–2.3 wt% Zn–0.7 wt% Ca–1 wt% Mn, obtained by hot pressing at 300 °C, with a yield stress of 229 MPa, an ultimate tensile strength of 278 MPa, a relative elongation of 10%, and a corrosion rate of 0.3 mm/year [29]. The manufacture of a number of medical products requires a thin sheet (up to 0.3 mm thick for biodegradable membranes), which can be obtained by hot rolling.

Therefore, the aim of this work is to determine the most optimal hot rolling regimes for the Mg–Zn–Ca–Mn alloy, ensuring the production of a defect-free thin sheet with the required strength–ductility balance and corrosion resistance.

2. Materials and Methods

2.1. Materials

High-purity Mg and Zn, as well as Mg-14 wt% Ca and Mg-2.7 wt% Mn master alloys, were used as the raw materials for the preparation of the alloys. Melting was carried out in a resistance furnace PT90/13 (LAC, Židlochovice, Czech Republic) with a graphite crucible under an Ar + SF_6 protective atmosphere. Purging with Ar was used to clean the melt. The prepared melt was cast into preheated graphite mold. The actual composition of the alloy obtained via EDS analysis was 96 wt% Mg–2.3 wt% Zn–0.7 wt% Ca–1 wt% Mn. The ingots were subjected to heat treatment to relieve stress at a temperature of 380 °C for 8 h. After this, the ingots were milling-machined to obtain plates of 54 mm wide, 70 mm long, and 7 mm thick. The resulting plates were rolled at two temperatures—300 and 400 °C. The plates were heated to the aforementioned temperatures, while the rolling mill rolls were maintained at room temperature. Between passes, the plates were held at the same temperatures for 10–15 min per pass. The diameter of the rolls was 80 mm, and the rolling speed was about 100 mm/s. The percentage reduction (relative draft) in a given pass was calculated using the following Equation:

$$\varepsilon = \frac{h_{k-1} - h_k}{h_{k-1}} \cdot 100\%, \quad (1)$$

where h_{k-1} and h_k are the plate thicknesses before and after the k-pass (k is the number of the pass, k = 0, 1, 2, . . .). The constant relative draft in the next passes was used. The final thickness of the plates was 0.24 ± 0.02 mm.

The total percentage reduction was calculated using the following Equation:

$$\varepsilon = \frac{h_0 - h_f}{h_0} \cdot 100\%, \quad (2)$$

where h_0 and h_f are the starting plate thickness and the plate thickness after rolling, respectively.

At 300 °C, the rolling process was carried out in 18 passes, and the average percentage reduction in a given pass was about 17%. At 400 °C, two rolling options were carried out: one part of the plates was rolled in 18 passes with an average percentage reduction in a given pass of about 18%, the other in 11 passes with an average percentage reduction in a given pass of about 26%. The sample designations that were selected for further research and testing are shown in Table 1.

After rolling, some plates were heated in an electric furnace at temperatures of 300 and 400 °C, held for 15 min and cooled in air.

Table 1. Characteristics of the studied samples.

Sample Designation	Total Percentage Reduction, %	Average Final Plate Thickness, mm
E6	63	2.60
E9	78	1.50
E12	88	0.83
E15	93	0.52
E17	96	0.30
E18	97	0.24

2.2. Sample Preparation

For microstructural studies, the longitudinal sections were etched using an etchant with the following composition: 11 g picric acid, 11 mL glacial acetic acid, and 100 mL ethanol.

For tensile testing, the dog-bone specimens of two types were cut from the rolled plates along the rolling direction (RD) using an electrical discharge wire cutting: (1) sub-size specimens with a total length of 12 mm, with the length and the width of the gauge part being 5 and 1.4 mm, respectively, and (2) full-scale specimens with a total length of 45 mm, with the length and the width of the gauge part being 20 and 3.5 mm, respectively. The thickness of the specimens corresponded to the thickness of the selected plates. Before tensile tests, the specimens' surfaces were not subjected to any grinding or polishing treatment. In this study, all the mechanical properties of the magnesium alloy were obtained by testing sub-size specimens, while full-size specimens were used selectively for comparative testing.

2.3. Tensile Test

Tensile tests were carried out using an Instron 5966 machine (Instron, Norwood, MA, USA). The strain rate was 2×10^{-3} s^{-1}. During testing, using built-in software, the stress–strain curves were recorded and the following mechanical characteristics were determined: the yield stress based on a yield plateau or a 0.2% yield point based on a residual deformation of 0.2% (YS), the ultimate tensile strength (UTS), and the relative elongation (RE). Three specimens of each condition were tested.

2.4. Structural Studies

The alloy phase composition was calculated according to the calculation of phase diagram (CALPHAD) method using Thermo-Calc software (v. 2016b, Thermo-Calc, Stockholm, Sweden) [30]. Furthermore, the Scheil–Gulliver solidification of the alloy was calculated [31]. The TCMG4 thermodynamic database (TCS Mg-based Alloys Database) was used for the calculation [32].

The samples' microstructure was analyzed using an Axio Observer D1m Carl Zeiss light microscope (LM) (Carl Zeiss, Oberkochen, Germany) with a built-in digital camera at a magnification of 500× and using a Tescan Vega 3 SBH scanning electron microscope (SEM) (Tescan, Brno, Czech Republic) in BSE mode with magnifications ranging from 200× to 2000×. The microstructure was examined in the rolling direction/normal direction (RD-ND) plane. The size of the grains was determined by the linear intercept method.

2.5. Corrosion Tests

Corrosion tests using the immersion method (weight loss) were carried out for the 300 °C-rolled plates with a total percentage reduction of 93% (E15) (Table 1). Some plates were also subjected to post-rolling heat treatment at 400 °C for 15 min. Using electrical discharge cutting, the samples with dimensions of 10 mm × 10 mm × 0.5 mm and a surface area of ~2 cm^2 were cut from the selected plates. The surfaces of the samples were cleaned using 320-grit sandpaper. A 400 mL Hanks' solution (PanEco, Moscow, Russia) was used as a corrosive medium. The test duration and ambient temperature were 192 h and 36.6–37 °C, respectively. The corrosion rate was determined using the standard method [33]. Weight loss was calculated according to the amount of hydrogen released during the tests and

collected in a burette (it was assumed that 1 mL of H_2 = 1 mg of Mg) [34,35]. The changes in pH were assessed using a pH meter HI83141 (Hanna Instruments, Woonsocket, RI, USA). Three as-rolled samples and three samples after heat treatment were tested. The volume of H_2 and pH was measured twice daily. The fitted curves were constructed on the basis of the measured results.

Polarization curves and EIS measurements were carried out in Hanks' solution at 37 °C in a standard three-electrode cell using an Autolab potentiostat/galvanostat (Metrohm, Herisau, Switzerland). The working electrode area was 0.13–0.25 cm^2, and an Ag/AgCl reference electrode (6.0733.100 Metrohm) and an auxiliary electrode made of platinum rod were also used. The scan rate was 1 mV/s. Electrochemical impedance spectroscopy (EIS) was performed at open circuit potential (OCP) in the frequency range from 0.1 Hz to 100 kHz with an amplitude of 0.01 V_{RMS}. All electrochemical results were recorded relative to the reference electrode and converted to SHE according to the relationship $E_{SHE} = E_{meas} - E_0$, with E_0 = +0.1985 V (Ag/AgCl vs. SHE at T = 37 °C).

3. Results and Discussion

3.1. Microstructure

Figure 1a shows the amount of phases vs. temperature for the 96.7 wt% Mg–2 wt% Zn–0.5 wt% Ca–0.8 wt% Mn alloy, calculated using Thermo-Calc software. The main phase in alloy is α-Mg and, for simplicity, only the part of graph up to 5 wt% is shown. In accordance with the calculation results, the alloy solidification starts at 641 °C. At 513 °C the α-Mn phase starts to form through peritectic reaction. Its content after solidification was 0.54 wt% but because of its high density, the volume fraction of this phase must be low. The two phases solidified from a liquid at 395 °C: 0.05 wt% for Mg_2Ca and 0.97 wt% for $Ca_2Mg_6Zn_3$. During further cooling, the amount of $Ca_2Mg_6Zn_3$ must increase and Mg_2Ca must disappear.

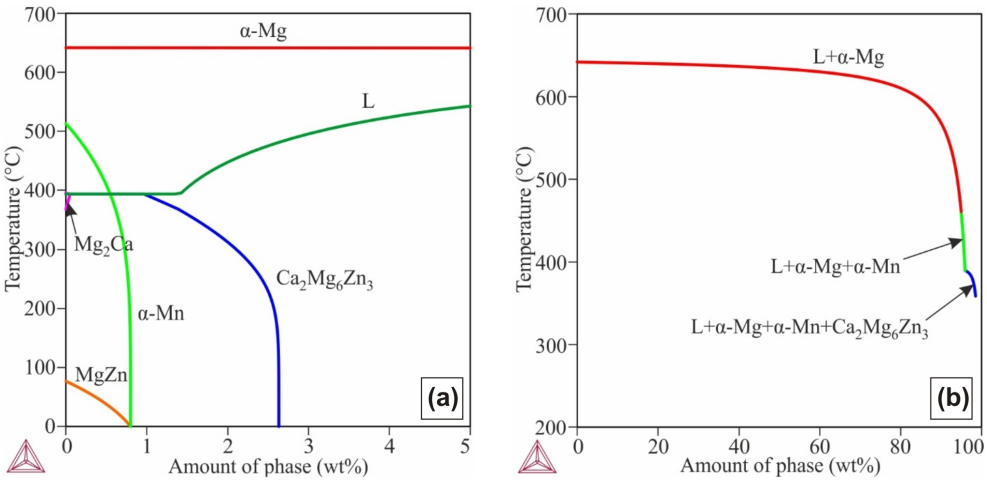

Figure 1. (**a**) The amount of phases vs. temperature and (**b**) the equilibrium and Scheil–Gulliver solidification pathways for a 96.7 wt% Mg–2 wt% Zn–0.5 wt% Ca–0.8 wt% Mn alloy.

Figure 1b shows the calculated Scheil–Gulliver solidification pathway for 96.7 wt% Mg–2 wt% Zn–0.5 wt% Ca–0.8 wt% Mn. It can be seen that the Mg_2Ca phase is not observed during the nonequilibrium solidification of an alloy with 2 wt% Zn, in opposition to the equilibrium solidification results and the actual alloy microstructure. The nonequilibrium solidus temperature was 364 °C, slightly lower than the equilibrium solidus temperature of 395 °C.

Figure 2 shows the LM images of the studied magnesium alloy's as-cast microstructure. The microstructure consists of α-Mg solid solution dendrites with an average size of 58 ± 32 μm, along the boundaries of which the Mg_2Ca, $Ca_2Mg_6Zn_3$, and α-Mn phases are located. This indicates that the cast alloy's phase composition corresponds to the

equilibrium phase calculated using Thermo-Calc software. More detailed studies of the microstructure of this alloy were carried out earlier [29].

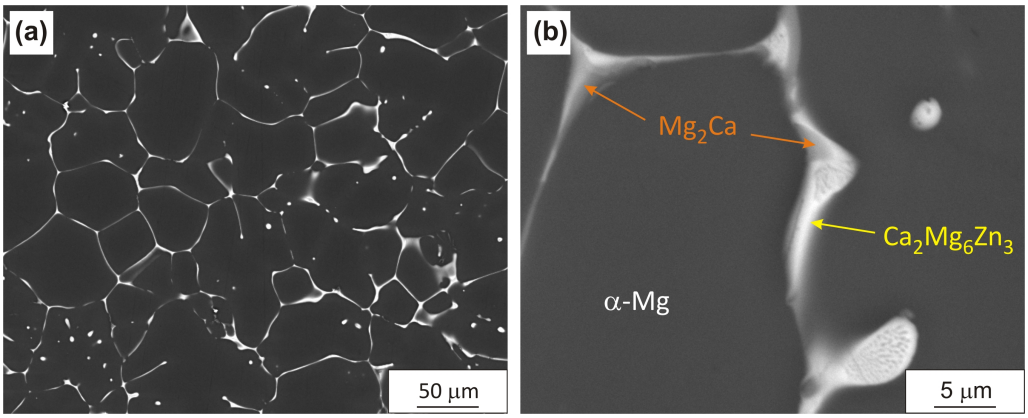

Figure 2. (**a**,**b**) Microstructure of the as-cast magnesium alloy (SEM).

As a result of the rolling, the secondary phase particles are crushed and pulled into lines along the rolling direction. The rolling temperature does not noticeably affect this process (Figures 3 and 4). Moreover, during hot rolling, the decomposition of the α-Mg solid solution and the precipitation of dispersoids of 100 nm in size are observed (see the inserts in Figures 3 and 4). Increasing the total percentage reduction intensifies the process of dispersoid precipitation.

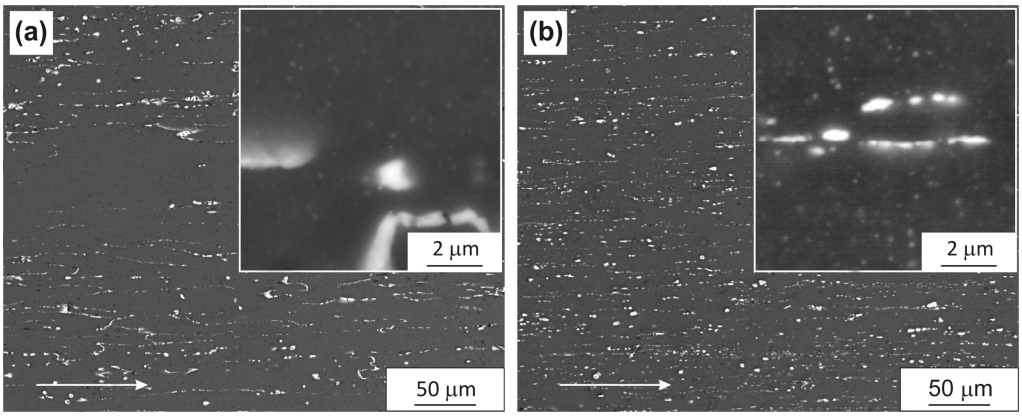

Figure 3. Microstructure of the RD-ND plane of a 300 °C-rolled magnesium alloy plates with different total percentage reductions (SEM): (**a**) E9; (**b**) E15. The arrow indicates the rolling direction.

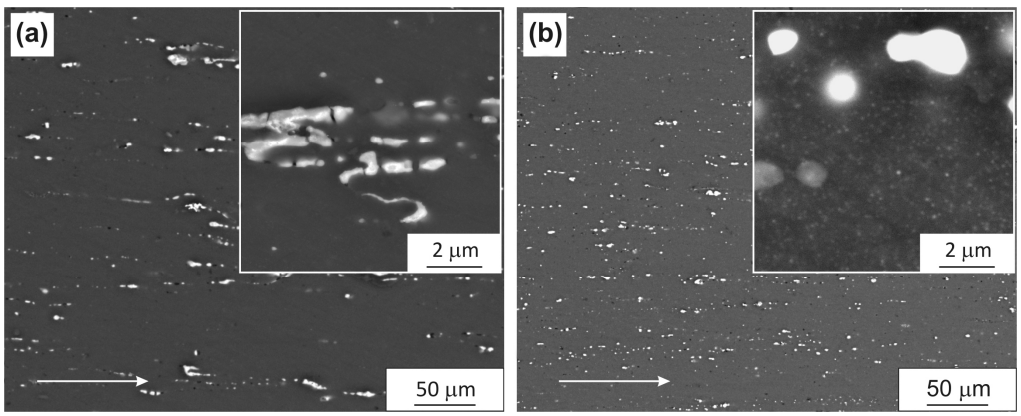

Figure 4. Microstructure of the RD-ND plane of a 400 °C-rolled magnesium alloy plates with different total percentage reductions (SEM): (**a**) E9; (**b**) E15. The arrow indicates the rolling direction.

Figures 5 and 6 show the typical LM images of the microstructure of the studied magnesium alloy plates rolled at different temperatures and with different total percentage reductions.

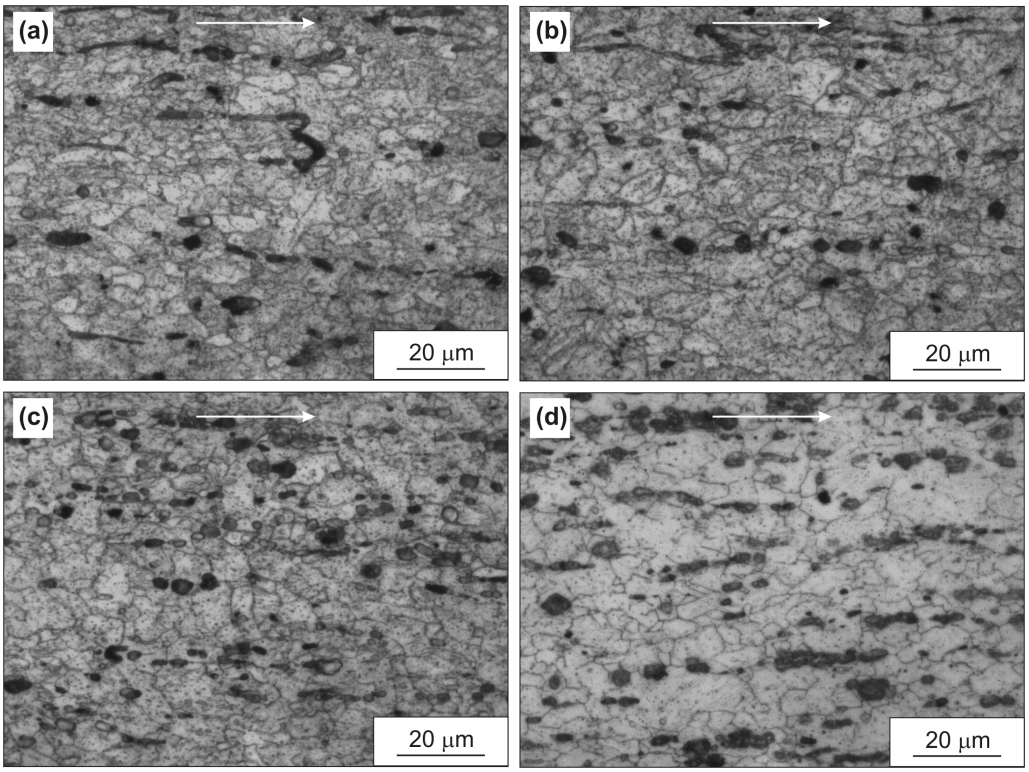

Figure 5. Microstructure of the RD-ND plane of a 300 °C-rolled magnesium alloy plates with different total percentage reductions (LM): (**a**) E9; (**b**) E12; (**c**) E15; (**d**) E18. The arrow indicates the rolling direction.

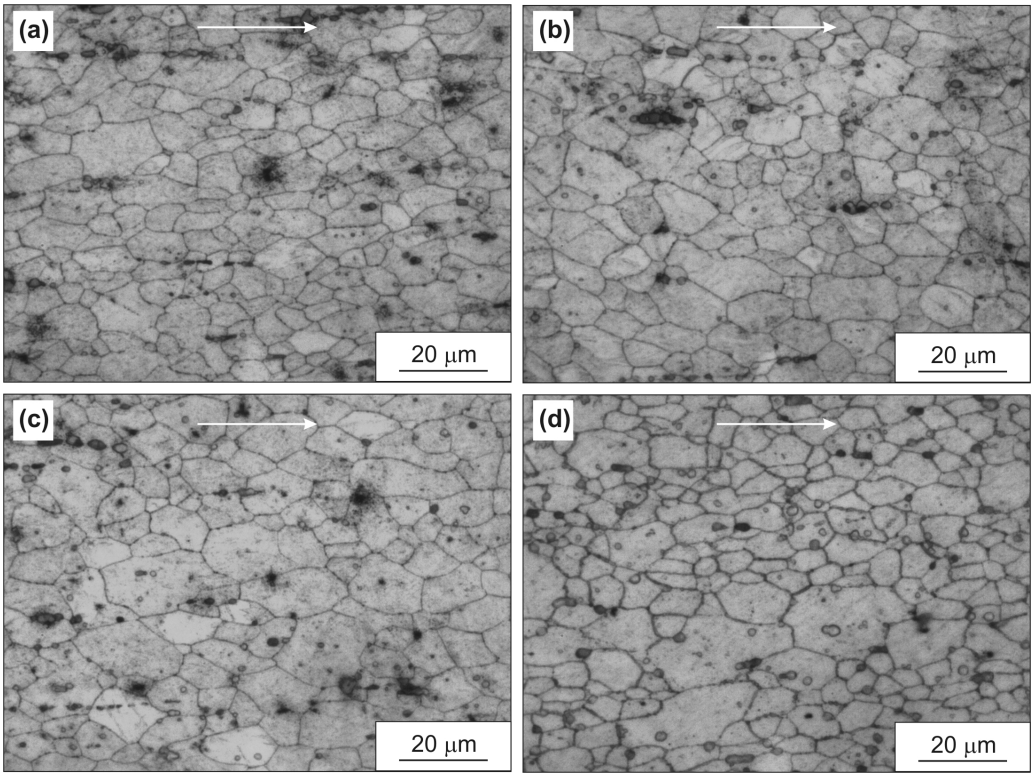

Figure 6. Microstructure of the RD-ND plane of a 400 °C-rolled magnesium alloy plates with different total percentage reductions (LM): (**a**) E9; (**b**) E12; (**c**) E15; (**d**) E18. The arrow indicates the rolling direction.

The microstructure of a 300 °C-rolled magnesium alloy plate is partially recrystallized, and the grain boundaries are strongly distorted (Figure 5a–c). It can be assumed that, during hot rolling, the microstructure formation in the alloy occurs according to the dynamic recrystallization mechanism. The degree of recrystallization increases only at high total percentage reductions (E18), and many grains acquire an equiaxed shape (Figure 5d). With an increase in the total percentage reduction from 78% (E9) to 97% (E18), the average grain size does not change and is about 7 μm. The microstructure contains grains of different sizes—from 2 to 21 μm, with smaller grains ranging in size from 2 to 8 μm being predominant.

The microstructure of a 400 °C-rolled magnesium alloy plate is completely recrystallized, regardless of the total percentage reduction, while the grain size is, on average, 1.4 times larger than after rolling at 300 °C, and the heterogeneity of the grains is preserved (Figure 6). The total percentage reduction and the average percentage reduction at a given pass do not affect the average grain size. The microstructure contains grains of different sizes—from 2 to 29 μm, with a predominance of grains ranging in size from 5 to 13 μm.

It should be taken into account that the plate is heated not only during the rolling process, but also between rolling passes. Therefore, the contribution of static recrystallization cannot be excluded. This circumstance apparently explains why the grain size does not depend on the total percentage reduction (degree of strain).

It is known that at low temperatures and extrusion rates, a bimodal microstructure with fine, dynamically recrystallized (DRXed) and coarse-textured non-DRXed grains with a strong basal texture is formed in Mg–Zn–Ca alloys. With increasing temperature and extrusion rates, a fully dynamically recrystallized coarse-grained microstructure is formed, while the basal texture dissipates [36–38]. The current results indicate the similarity of the microstructure formation mechanisms in the 96 wt% Mg–2.3 wt% Zn–0.7 wt% Ca–1 wt% Mn alloy during hot extrusion and hot rolling.

3.2. Tensile Test

Table 2 shows the averaged values (over three specimens) of the rolled plates' mechanical properties obtained during tensile testing vs. the rolling temperature, and the total percentage reduction or the average percentage reduction in a given pass. The typical tensile stress–strain curves are shown in Figure 7.

Table 2. Mechanical properties of the hot-rolled magnesium alloy plates.

Sample Designation	YS, MPa	UTS, MPa	RE, %
Rolling temperature of 300 °C and average percentage reduction at a given pass of about 17%			
E6	227 ± 23	304 ± 2	6.0 ± 1.0
E9	297 ± 18	325 ± 11	4.0 ± 1.0
E9 *	-	215 ± 21	0
E15	278 ± 18	315 ± 4	7.0 ± 1.0
E17	292 ± 5	308 ± 3	3.0 ± 1.5
E17 *	284 ± 11	309 ± 3	2.5 ± 0.5
E18	291 ± 9	307 ± 2	5.0 ± 1.0
Rolling temperature of 400 °C and average percentage reduction at a given pass of about 16%			
E9	249 ± 17	259 ± 19	1.0 ± 0.5
E12	296 ± 13	309 ± 13	2.5 ± 0.5
E15	293 ± 3	301 ± 8	2.5 ± 0.5
E18	276 ± 6	302 ± 12	3.0 ± 0.5
E18 *	297 ± 8	322 ± 11	3.5 ± 0.5
Rolling temperature of 400 °C and average percentage reduction at a given pass of about 26%			
E9	251 ± 20	251 ± 20	0
E15	264 ± 51	269 ± 53	3.0 ± 2.0
E18	299 ± 23	322 ± 12	2.3 ± 1.5
E18 *	276 ± 22	312 ± 14	1.8 ± 0.8

Note: All results are obtained from testing sub-size specimens, except (*), which represents full-size specimens.

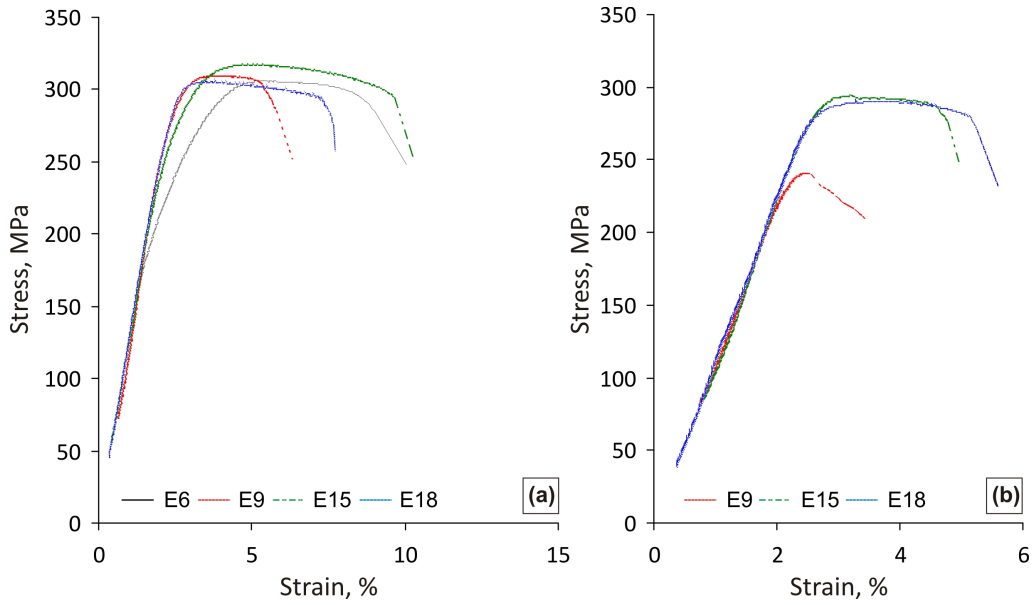

Figure 7. Tensile curves of the magnesium alloy samples rolled at temperatures of (**a**) 300 °C and (**b**) 400 °C.

The samples from plates rolled at a temperature of 300 °C with total percentage reductions from 78% (E9) to 97% (E18) have similar mechanical properties: the YS, the UTS, and the RE averaged at 290 MPa, 315 MPa, and 5%, respectively. The comparative tensile tests of the sub-size and full-scale specimens showed that for high total percentage reductions (from E12 to E18), the values of both strength and elongation do not depend on the geometry of the specimen (Table 2). On the contrary, at low total percentage reductions (E6 and E9), the failure of full-scale specimens occurred in the elastic region. This can be explained as follows. The plates after low total percentage reductions contain many macrodefects (cracks), which heal with increases in the total percentage reduction (the process of healing cracks during rolling has been previously studied [39]). Thus, when testing the full-scale specimens, there is a higher probability of a defect occurring in the specimen's gauge part, which will lead to premature brittle fracture.

With an increase in rolling temperature to 400 °C, the strength properties of the alloy at the same total percentage reductions do not change on average, but there is a tendency for the elongation to decrease to about 3%. It was expected that the formation of a completely recrystallized microstructure during rolling at 400 °C would lead to an increase in elongation. The results obtained, however, indicate a decrease in elongation. Apparently, this is not due to the microstructure type, but to the formation of cracks during rolling, which lead to the premature failure of the specimen. This is evidenced by the observed scatter in the values of the mechanical characteristics of the samples rolled at a temperature of 400 °C, as well as the fracture of some of them in the elastic region during testing. In addition, an increase in the average total percentage reduction in a given pass from 16 to 26% leads to a significant increase in the spread of the strength characteristics. This can be explained by the intensification of sheet cracking during rolling due to the very high relative elongation in subsequent passes.

To improve ductility (elongation), the 96 wt% Mg–2.3 wt% Zn–0.7 wt% Ca–1 wt% Mn alloy was annealed after rolling. A sample rolled at 300 °C to a total percentage reduction of 93% (E15) was selected. The mechanical properties of the rolled samples following annealing are provided in Table 3. The typical tensile curves are shown in Figure 8. Annealing at a temperature of 300 °C for 15 min led to a slight (6–9%) decrease in strength, while the elongation did not change and amounted to about 6%. Annealing at a temperature of 400 °C for 15 min led to a significant decrease in strength (by 16–30%), while the elongation increased significantly (up to 17%). This change in mechanical properties can

be associated with a change in the microstructure (Figure 9), namely an increase in grain size to 5–12 μm as a result of collective recrystallization. The movement of dislocations is facilitated, which is confirmed by the appearance of a yield plateau on the tensile curve. Despite some softening after annealing, the alloy meets the requirements for medicine in terms of strength (YS is 200 MPa) and ductility (RE is 17%).

Table 3. Mechanical properties of a 300 °C-rolled magnesium alloy plate with a total percentage reduction of 93% (E15) following annealing.

Annealing Regime	YS, MPa	UTS, MPa	ER, %
300 °C for 15 min	269 ± 5	283 ± 5	6.0 ± 1.0
400 °C for 15 min	200 ± 1	261 ± 1	17.5 ± 0.5

Note: All results are obtained from testing sub-size specimens.

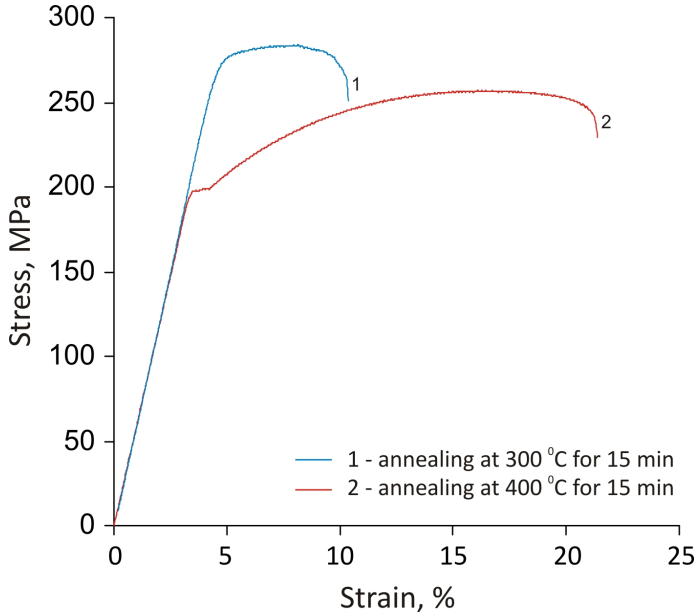

Figure 8. Tensile curves of the magnesium alloy samples after rolling at a temperature of 300 °C to a total percentage reduction of 93% (E15) following annealing.

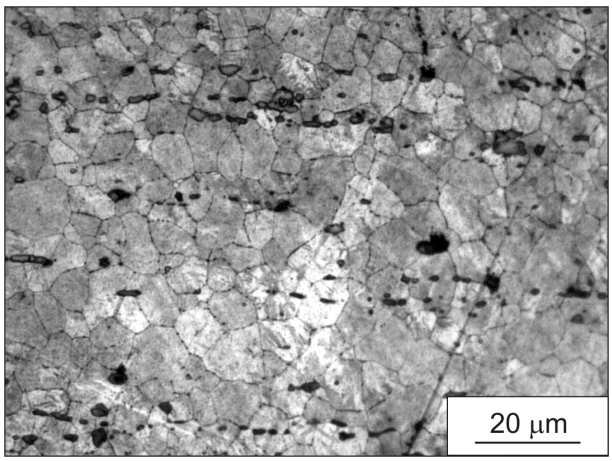

Figure 9. The magnesium alloy microstructure after rolling at a temperature of 300 °C to a total percentage reduction of 93% (E15) following annealing at 400 °C for 15 min (LM).

In the future, to optimize the hot-rolling process modes, it is advisable to obtain a hot-rolling model of an magnesium alloy using the Zener–Hollomon parameter, which

describes the combined effect of temperature and strain rate on the deformation behavior of the material, as has been successfully accomplished for many metals and alloys [40,41].

3.3. Corrosion Tests

Figure 10a illustrates the variation in the amount of hydrogen released during a corrosion testing of the alloy after rolling at 300 °C, as well as after post-rolling annealing at 400 °C for 15 min. It is worth noting that the highest intensity of the hydrogen release was observed during the initial hours of the corrosion test due to the absence of a corrosion product layer on the surface of the alloy. This layer acts as a barrier against the contact of the metal surface and the corrosive medium. After the formation of a layer of corrosion products, the intensity of hydrogen evolution decreases significantly. This trend is observed in both the as-rolled alloy and the alloy annealed up to the end of the corrosion test. The observed behavior is typical for the investigated alloy after hot extrusion [29], where the corrosion rate decreases with increasing holding time. The corrosion rate determined from the results of corrosion tests for the alloy rolled at 300 °C was 0.54 ± 0.31 mm/year. Post-rolling annealing at 400 °C for 15 min resulted in a significant reduction in the corrosion rate, reaching a value of 0.19 ± 0.06 mm/year. It is worth noting that the as-rolled alloy showed a high confidence limit due to significant discrepancies between individual corrosion rate values.

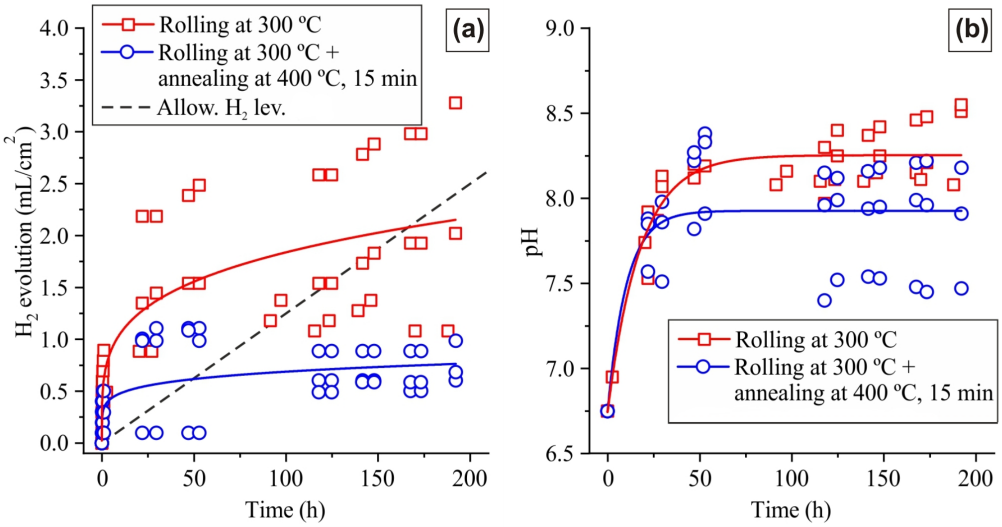

Figure 10. (**a**) The amount of hydrogen released and (**b**) the change in the pH of the medium during corrosion testing in the medium of Hank's solution at a temperature of 37 °C for 192 h; the dashed line summarizes the data of Kraus et al. [42].

The release of H_2 can cause gas pockets to form in tissues after implant installation. As Kraus et al. pointed out in their study on rats, tissues can carry away a maximum of 0.295 mL/cm^2 of H_2 per day [42]. The dashed line in Figure 10a indicates the acceptable hydrogen level over time. The as-rolled alloy initially provides a hydrogen level up to three times higher than what is considered acceptable. However, after approximately 170 h of testing, the hydrogen level becomes acceptable. Similarly, in the case of the annealed alloy, an acceptable level is observed after 50 h of experimentation. This indicates that the gas pocket volume in the tissues may be lower for the annealed alloy, which promotes the good connectivity of osteocytes with the implant surface and helps to maintain implant integrity [42].

The heat treatment led to a notable reduction in the confidence limit, as the corrosion rate values observed in each trial for the annealed alloy were very similar. Additionally, after annealing, the time during which the released hydrogen volume exceeds the acceptable level is only 50 h. This issue can be addressed by employing a protective coating, which effectively reduces the hydrogen level during the initial postoperative period. It is possible

that the higher corrosion rate in the as-rolled plates was due to the formation of a strong crystallographic texture, residual stresses, and precipitates during the rolling process [43,44]. However, after annealing, the stress is relieved, and recrystallization processes develop. After annealing, the strength of the alloy decreases while its ductility increases compared to its as-rolled condition. This is due to stress relief, texture weakening, and an increase in grain size. As a result, the corrosion rate decreases, and the corrosion behavior becomes more stable (with a lower confidence limit). It is worth noting that the alloy with only post-rolling annealing meets the corrosion rate requirement of less than 0.5 mm/year that is typical for biodegradable implants [14].

It is a well-established fact that the corrosion rate of an alloy is dependent upon the alteration in pH levels within the corrosive medium [17,23]. Consequently, an elevated pH value is indicative of an increased corrosion rate, and vice versa. The alteration in the pH of the corrosive medium during the corrosion test is illustrated in Figure 10b. In particular, at the commencement of the test, the pH of the as-rolled alloy increased from 6.7 to 8.2 as a consequence of the release of hydrogen in the form of gas and the subsequent rise in the concentration of hydroxide anions [35]. Subsequently, the pH remained unaltered for the entirety of the 50 h immersion period and until the end of the corrosion test. This indicates that following a 50 h immersion period, a corrosion products film was fully formed, resulting in a near-constant corrosion rate. The behavior of the annealed alloy was observed to be similar to that of the as-rolled alloy, with a pH of 7.9 after 50 h of immersion, which was slightly lower than that of the as-rolled alloy. This indicates that the corrosion rate of the rolled alloy is reduced by annealing, as evidenced by the pH value of the corrosion media decreasing in comparison with the as-rolled alloy.

Figure 11 shows the polarization curves obtained for alloy samples rolled at 300 °C and heat-treated at 400 °C for 15 min after rolling. The surface of the samples parallel and perpendicular to the rolling direction was analyzed. The corrosion current density and corrosion rate obtained using the Tafel fitting corrosion potential are provided in Table 4. The corrosion potential was near −1.3 V for all the samples. However, the corrosion rate differed by five to ten times for the sample surfaces located parallel and perpendicular to rolling direction. Heat treatment led to a nearly two times decrease in the corrosion rate on the surface parallel to the rolling direction via the weakening of crystallographic texture and the revealing of residual stresses. The corrosion rate on the surface perpendicular to the rolling direction following heat treatment is also reduced, albeit to a lesser extent. Because a greater fraction of the samples surface is located parallel to the rolling direction, the overall effect of heat treatment is better defined.

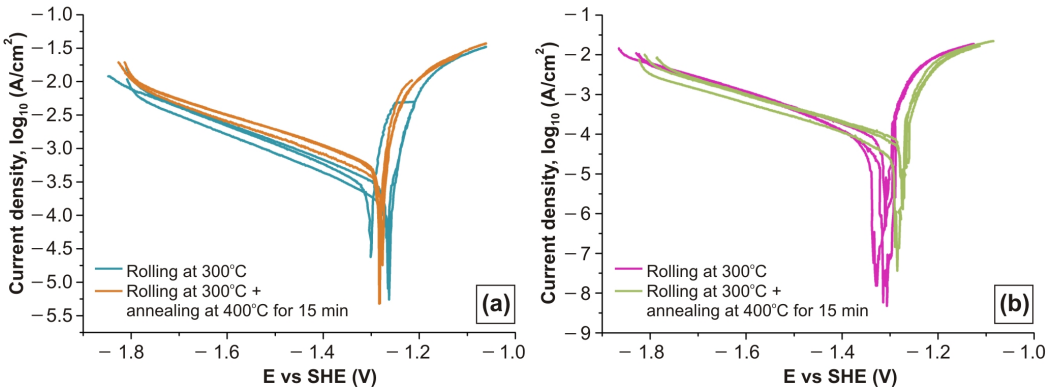

Figure 11. Polarization curves of as-rolled alloy at 300 °C and heat-treated alloy at 400 °C during 15 min after rolling alloy samples: (**a**) perpendicular to rolling direction; (**b**) parallel to rolling direction.

Representative EIS spectra of various samples are shown in Figures 12 and 13. Mg-based alloys are highly reactive in aqueous solutions containing Cl^- ions even when the applied polarization is only slight; therefore, a steady state is difficult to achieve for them, which complicates the accurate quantitative evaluation of EIS results. The impedance

values obtained at low frequencies contain a significant amount of noise and dispersion, which is associated with unstable Mg corrosion processes such as the relaxation of adsorbed species or pitting corrosion [45,46]. The electrochemical interface can be described by a Randles equivalent circuit (insert in Table 5) modified with inductance (L) and resistance (R), where a constant-phase element (CPE) is used instead of capacitance (C) [47]. The equivalent circuit (insert in Table 5) includes the solution resistance between the control sample and the working electrode (R_1), a constant-phase element (CPE1) that is parallel to the surface film charge transfer resistance, which includes both charge and mass transfer aspects (R_{ct}), and an inductance (L) with a resistance (R_L). The presence of an inductive loop at low frequencies is explained by previous studies [48] on the occurrence of pitting corrosion, which is clearly visible in the images displaying the surface of the samples after immersion corrosion tests (Figure 14).

Table 4. Characteristics of potentials, corrosion currents, and corrosion rate (CR).

Condition	Orientation	E_{corr} vs. SHE, V	J, mA/cm^2	CR, mm/y
Rolling at 300 °C	Perpendicular to RD	−1.28 ± 0.02	0.107 ± 0.001	2.46 ± 0.01
Rolling at 300 °C followed by annealing at 400 °C for 15 min	Perpendicular to RD	−1.28 ± 0.01	0.102 ± 0.004	2.34 ± 0.08
Rolling at 300 °C	Parallel to RD	−1.32 ± 0.01	0.018 ± 0.005	0.41 ± 0.10
Rolling at 300 °C followed by annealing at 400 °C for 15 min	Parallel to RD	−1.27 ± 0.01	0.010 ± 0.004	0.23 ± 0.09

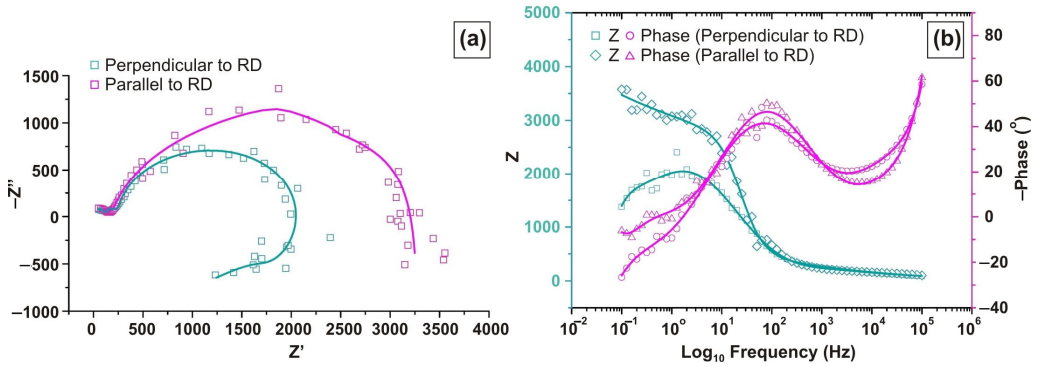

Figure 12. EIS measurement data for the 300 °C -rolled samples: (**a**) Nyquist plot; (**b**) phase angle and Bode plot.

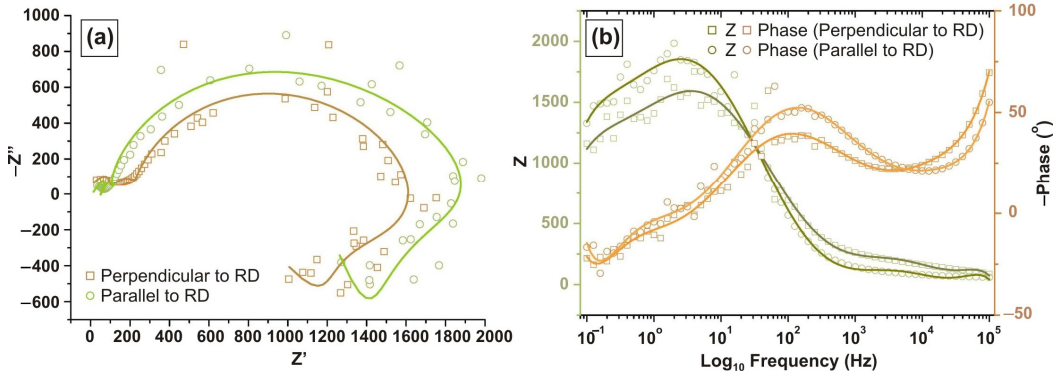

Figure 13. EIS measurement data for samples after rolling at 300 °C followed by annealing at 400 °C for 15 min: (**a**) Nyquist plot; (**b**) phase angle and Bode plot.

Table 5. Corrosion product values for the equivalent scheme of Mg alloy corrosion.

Parameters	Rolling at 300 °C		Rolling at 300 °C Followed Annealing at 400 °C for 15 min	
	Perpendicular to RD	Parallel to RD	Perpendicular to RD	Parallel to RD
R_1, (Ω cm^2)	180	178	181	180
R_{ct}, (kΩ cm^2)	3.13	5.63	2.4	2.54
R_L, (kΩ cm^2)	3.5	6.56	2.51	3.95
CPE1, (S Sec^n cm^{-2})	$5.33 \cdot 10^{-6}$	$6.37 \cdot 10^{-6}$	$2.73 \cdot 10^{-6}$	$2.7 \cdot 10^{-6}$
n1	0.94	0.861	0.994	0.997
L, (H)	$5.5 \cdot 10^{-2}$	$2.71 \cdot 10^{-1}$	$1.47 \cdot 10^{-2}$	0.9

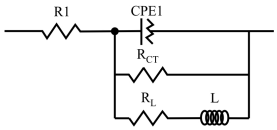

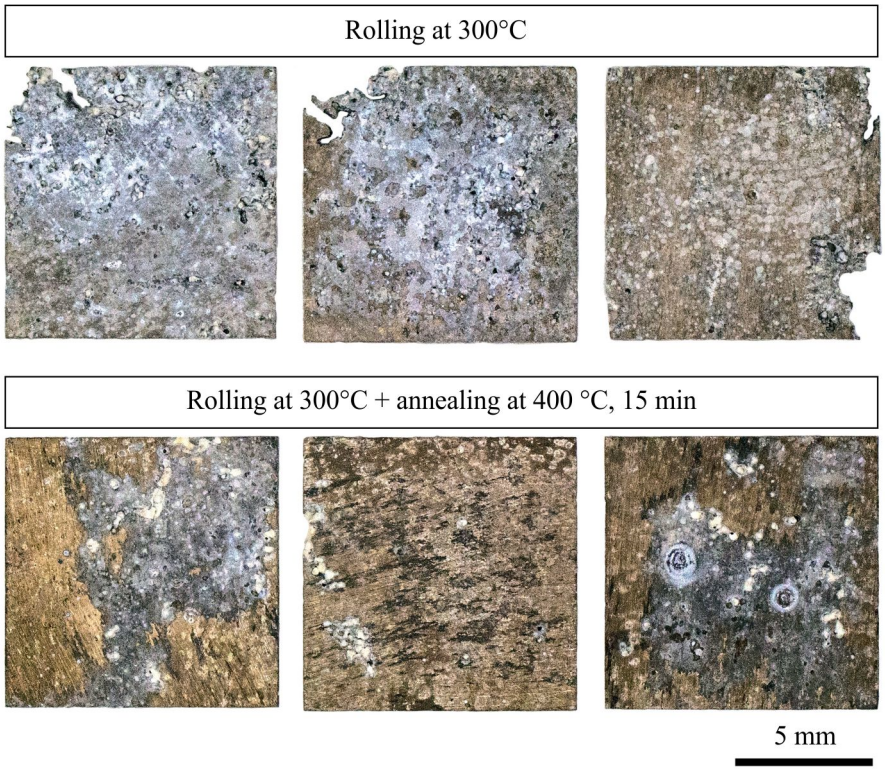

Figure 14. Samples' surfaces (parallel to RD) after immersion corrosion tests.

The Nyquist diagram (Figure 12a) shows that the rolled samples exhibit an anisotropy of properties depending on their orientation relative to the rolling direction. Thus, the sample whose surface is perpendicular to the rolling direction exhibits a lower resistance (R_{ct}) than the sample whose surface is open and parallel to the rolling direction. This is also confirmed by the dependencies in the Bode diagram (Figure 12b), where in the low-frequency region, the total resistance (Z) differs by more than two times. This agrees well with the immersion test data, as follows from Figure 14 for the rolled samples; strong corrosion foci are recorded on the end plates. The EIS results for the samples that underwent heat treatment after rolling (Figure 13) confirm the observation of increased corrosion resistance, which may be associated with the weakening of the crystallographic texture and the manifestation of residual stresses. Thus, the Nyquist and Bode diagrams show a less significant change in resistance (R_{ct}) depending on the orientation of the sample plane relative to the rolling direction, which is also consistent with the data after immersion tests (Figure 14), where the corrosion products were uniformly distributed over the surface of the samples and no deep corrosion cavities were observed that disrupt the rectangular shape of the sample.

The EIS data presented in Figures 12 and 13 also show inductive responses corresponding to the desorption of the corrosion products film. Thus, the Nyquist diagrams are characterized by an inductive loop below the semicircle at low frequencies. This appearance of the inductive loop, which is described by the elements (R_L) and (L) of the equivalent circuit, is characteristic of the formation of pits [48] and the destruction of the layer of corrosion products, which the authors [47,49,50] of the previous studies associate with the relaxation processes of intermediate compounds adsorbed on the alloy surface. This is also confirmed by the results of immersion tests. Thus, in Figure 14, in the areas of corrosion damage to the alloy, areas of active pitting, and the desorption of corrosion products are observed.

As is known [51], due to the participation of anodic hydrogen evolution processes or the negative difference effect in Mg corrosion, the corrosion rate of Mg alloys estimated using the Tafel slope and EIS is not accurate. Unlike other metals, the Stern–Geary relationship is not observed during Mg corrosion, which is associated with an increase in H_2 evolution in the cathodic stage with an increase in anodic polarization; this phenomenon is commonly known as the negative difference effect (NDE). Considering that electrochemical methods are currently not autonomous when studying the interaction of Mg and electrolyte, knowledge of the Tafel parameters is necessary to convert the polarization resistance into a corrosion rate, while gravimetric mass loss, H_2 collection, and corrosion product analysis methods are also used to correlate the measurements of the obtained polarization curve and impedance analysis data.

4. Conclusions

The findings of the study regarding the influence of the hot rolling process on the microstructure and mechanical and corrosion properties of the plates of magnesium alloy 96 wt% Mg–2.3 wt% Zn–0.7 wt% Ca–1 wt% Mn established the following:

(1) Increasing the rolling temperature from 300 to 400 °C increases the fraction of recrystallized grains in the microstructure, and after rolling at 400 °C, the microstructure is fully recrystallized.

(2) The plates rolled at 300 °C to high total percentage reductions of 93–97% have the best strength–ductility balance: the average yield stress and the ultimate tensile strength were 285 MPa and 310 MPa, respectively, and the elongation was 5%.

(3) Post-rolling annealing of the rolled alloy improves its ductility: after rolling at 300 °C followed by annealing at 400 °C, the yield stress, the ultimate tensile strength, and the elongation averaged 200 MPa, 260 MPa, and 17%, respectively.

(4) The corrosion rate of the rolled alloy and the post-rolling annealed alloy is 0.54 and 0.19 mm/year, respectively. The high corrosion rate of rolled plates may be attributed to the formation of a strong crystallographic texture, residual stresses, and precipitates in the alloy microstructure. Post-rolling weakens the influence of the mentioned factors, thereby decreasing the corrosion rate.

The sheets obtained with only post-rolling annealing meet the requirements for biodegradable materials (corrosion rate <0.5 mm/year) and can be recommended for the production of biodegradable implants.

Author Contributions: Conceptualization, V.E.B., A.A.K. and K.S.S.; funding acquisition, A.A.K. and K.S.S., investigation, S.O.R., V.A.B., A.V.L., S.V.P., D.V.T. and V.V.Y.; formal analysis V.A.B., S.V.P., D.V.T. and V.V.Y., methodology, V.E.B., V.A.B. and A.V.L.; resources, V.E.B.; validation, A.V.L., S.V.P. and V.E.B.; visualization: V.A.B., D.V.T., V.V.Y. and S.O.R.; writing—original draft preparation, S.O.R.; writing—review and editing, V.E.B., V.A.B., S.V.P., D.V.T., V.V.Y., A.A.K. and K.S.S. All authors have read and agreed to the published version of the manuscript.

Funding: The authors are grateful to the Ministry of Science and Higher Education of the Russian Federation for their financial support under the Megagrant (#075-15-2022-1133). The mechanical tests were carried out with the financial support of the Russian Science Foundation (project #22-79-10299, https://rscf.ru/project/22-79-10299/). The corrosion tests were carried out during the

implementation of the strategic project, «Biomedical materials and bioengineering», within the framework of the Strategic Academic Leadership Program «Priority 2030» at NUST «MISIS».

Data Availability Statement: The original contributions presented in the study are included in the article, further inquiries can be directed to the corresponding author.

Conflicts of Interest: The authors declare no conflicts of interest.

References

1. Vujović, S.; Desnica, J.; Stanišić, D.; Ognjanović, I.; Stevanovic, M.; Rosic, G. Applications of biodegradable magnesium-based materials in reconstructive oral and maxillofacial surgery: A review. *Molecules* **2022**, *27*, 5529. [CrossRef] [PubMed]
2. Kumar, A.; Pandey, P.M. Development of Mg based biomaterial with improved mechanical and degradation properties using powder metallurgy. *J. Magnes. Alloys* **2020**, *8*, 883–898. [CrossRef]
3. Ahuja, N.; Grewal, N.S.; Kumar, K.; Batra, U. Investigating in-vitro degradation, fatigue behavior, and fracture toughness of electrical discharge-processed Mg alloys for biodegradable implant applications. *Int. J. Lightweight Mater. Manuf.* **2024**, *7*, 293–307. [CrossRef]
4. Zheng, B.; Wang, J.; Wu, W.; Ou, J. Functionalized Coatings on Degradable Magnesium Alloys for Orthopedic Implants: A Review. *Trans. Indian Inst. Met.* **2023**, *76*, 613–627. [CrossRef]
5. Rogachev, S.O.; Bazhenov, V.E.; Komissarov, A.A.; Ten, D.V.; Li, A.V.; Andreev, V.A.; Statnik, E.S.; Sadykova, I.A.; Plegunova, S.V.; Yushchuk, V.V.; et al. High strength and ductility in a new Mg–Zn–Ga biocompatible alloy by drawing and rotary forging. *Results Mater.* **2024**, *21*, 1000524. [CrossRef]
6. Rogachev, S.O.; Bazhenov, V.E.; Komissarov, A.A.; Li, A.V.; Ten, D.V.; Yushchuk, V.V.; Drobyshev, A.Y.; Shin, K.S. Effect of hot rolling on structure and mechanical properties of Mg–Y–Zn–Mn alloys. *Metals* **2023**, *13*, 223. [CrossRef]
7. Nakata, T.; Xu, C.; Abe, R.; Geng, L.; Kamado, S. Unexpectedly formed strong basal texture in a rolled Mg-Zn-Ca-Mn alloy sheet. *Mater. Charact.* **2023**, *203*, 113101. [CrossRef]
8. Ou, K.-L.; Chen, C.-C.; Chiu, C. Production of Oxide Dispersion Strengthened Mg-Zn-Y Alloy by Equal Channel Angular Pressing of Mechanically Alloyed Powder. *Metals* **2020**, *10*, 679. [CrossRef]
9. Nakata, T.; Xu, C.; Ito, Y.; Kamado, S. Role of homogenization on tensile properties and microstructures in a dilute Mg–Zn–Ca–Mn alloy sheet. *Mater. Sci. Eng. A* **2022**, *833*, 142541. [CrossRef]
10. Liu, C.; Chen, X.; Chen, J.; Atrens, A.; Pan, F. The effects of Ca and Mn on the microstructure, texture and mechanical properties of Mg-4 Zn alloy. *J. Magnes. Alloys* **2021**, *9*, 1084–1097. [CrossRef]
11. Zhao, L.-Q.; Wang, C.; Chen, J.-C.; Ning, H.; Yang, Z.-Z.; Xu, J.; Wang, H.-Y. Development of weak-textured and high-performance Mg–Zn–Ca alloy sheets based on Zn content optimization. *J. Alloys Compd.* **2020**, *849*, 156640. [CrossRef]
12. Nie, K.; Zhu, Z.; Munroe, P.; Deng, K.; Han, J. The effect of Zn/Ca ratio on the microstructure, texture and mechanical properties of dilute Mg–Zn–Ca–Mn alloys that exhibit superior strength. *J. Mater. Sci.* **2020**, *55*, 3588–3604. [CrossRef]
13. Sun, Y.; Zhang, B.; Wang, Y.; Geng, L.; Jiao, X. Preparation and characterization of a new biomedical Mg–Zn–Ca alloy. *Mater. Des.* **2012**, *34*, 58–64. [CrossRef]
14. Chen, Y.; Xu, Z.; Smith, C.; Sankar, J. Recent advances on the development of magnesium alloys for biodegradable implants. *Acta Biomater.* **2014**, *10*, 4561–4573. [CrossRef]
15. Gu, X.-N.; Li, S.-S.; Li, X.-M.; Fan, Y.-B. Magnesium based degradable biomaterials: A review. *Front. Mater. Sci.* **2014**, *8*, 200–218. [CrossRef]
16. Radha, R.; Sreekanth, D. Insight of magnesium alloys and composites for orthopedic implant applications—A review. *J. Magnes. Alloys* **2017**, *5*, 286–312. [CrossRef]
17. Bakhsheshi-Rad, H.R.; Idris, M.H.; Abdul-Kadir, M.R.; Ourdjini, A.; Medraj, M.; Daroonparvar, M.; Hamzah, E. Mechanical and bio-corrosion properties of quaternary Mg–Ca–Mn–Zn alloys compared with binary Mg–Ca alloys. *Mater. Des.* **2014**, *53*, 283–292. [CrossRef]
18. Ibrahim, H. Mechanical and In Vitro Corrosion Properties of a Heat-Treated Mg-Zn-Ca-Mn Alloy as a Potential Bioresorbable Material. *Adv. Metall. Mater. Eng.* **2017**, *1*, 1–7. [CrossRef]
19. Yandong, Y.; Shuzhen, K.; Teng, P.; Jie, L.; Caixia, L. Effects of Mn Addition on the Microstructure and Mechanical Properties of As-cast and Heat-Treated Mg-Zn-Ca Bio-magnesium Alloy. *Metallogr. Microstruct. Anal.* **2015**, *4*, 381–391. [CrossRef]
20. She, J.; Pan, F.S.; Guo, W.; Tang, A.T.; Gao, Z.Y.; Luo, S.Q.; Song, K.; Yu, Z.W.; Rashad, M. Effect of high Mn content on development of ultra-fine grain extruded magnesium alloy. *Mater. Des.* **2016**, *90*, 7–12. [CrossRef]
21. Cho, D.H.; Lee, B.W.; Park, J.Y.; Cho, K.M.; Park, I.M. Effect of Mn addition on corrosion properties of biodegradable Mg-4Zn-0.5Ca-xMn alloys. *J. Alloys Compd.* **2017**, *695*, 1166–1174. [CrossRef]
22. Zhang, B.; Hou, Y.; Wang, X.; Wang, Y.; Geng, L. Mechanical properties, degradation performance and cytotoxicity of Mg–Zn–Ca biomedical alloys with different compositions. *Mater. Sci. Eng. C* **2011**, *31*, 1667–1673. [CrossRef]
23. Fazel Anvari-Yazdi, A.; Tahermanesh, K.; Hadavi, S.M.; Talaei-Khozani, T.; Razmkhah, M.; Abed, S.M.; Mohtasebi, M.S. Cytotoxicity assessment of adipose-derived mesenchymal stem cells on synthesized biodegradable Mg-Zn-Ca alloys. *Mater. Sci. Eng. C* **2016**, *69*, 584–597. [CrossRef] [PubMed]

24. Gopi, K.R.; Shivananda Nayaka, H.; Sahu, S. Microstructural Evolution and Strengthening of AM90 Magnesium Alloy Processed by ECAP. *Arab. J. Sci. Eng.* **2017**, *42*, 4635–4647. [CrossRef]
25. Tong, L.B.; Zheng, M.Y.; Xu, S.W.; Kamado, S.; Du, Y.Z.; Hu, X.S.; Wu, K.; Gan, W.M.; Brokmeier, H.G.; Wang, G.J.; et al. Effect of Mn addition on microstructure, texture and mechanical properties of Mg–Zn–Ca alloy. *Mater. Sci. Eng. A* **2011**, *528*, 3741–3747. [CrossRef]
26. Geng, L.; Zhang, B.P.; Li, A.B.; Dong, C.C. Microstructure and mechanical properties of Mg–4.0Zn–0.5Ca alloy. *Mater. Lett.* **2009**, *63*, 557–559. [CrossRef]
27. Bian, D.; Zhou, W.; Deng, J.; Liu, Y.; Li, W.; Chu, X.; Xiu, P.; Cai, H.; Kou, Y.; Jiang, B.; et al. Development of magnesium-based biodegradable metals with dietary trace element germanium as orthopaedic implant applications. *Acta Biomater.* **2017**, *64*, 421–436. [CrossRef]
28. Zhang, B.; Wang, Y.; Geng, L.; Lu, C. Effects of calcium on texture and mechanical properties of hot-extruded Mg–Zn–Ca alloys. *Mater. Sci. Eng. A* **2012**, *539*, 56–60. [CrossRef]
29. Bazhenov, V.E.; Li, A.V.; Komissarov, A.A.; Koltygin, A.V.; Tavolzhanskii, S.A.; Bautin, V.A.; Voropaeva, O.O.; Mukhametshina, A.M.; Tokar, A.A. Microstructure and mechanical and corrosion properties of hot-extruded Mg–Zn–Ca–(Mn) biodegradable alloys. *J. Magnes. Alloys* **2021**, *9*, 1428–1442. [CrossRef]
30. Andersson, J.O.; Helander, T.; Höglund, L.; Shi, P.F.; Sundman, B. Thermo-Calc & DICTRA, Computational tools for materials science. *Calphad* **2002**, *26*, 273–312. [CrossRef]
31. Scheil, E. Bemerkungen zur Schichtkristallbildung. *Zeit. Metallkunde.* **1942**, *34*, 70–72. [CrossRef]
32. Thermo-Calc software TCMG4 Magnesium Alloys Database Version 4. Available online: https://www.engineering-eye.com/THERMOCALC/details/db/pdf/thermo-calc/02/tcmg4_extended_info.pdf (accessed on 1 February 2024).
33. *ASTM Standard G1–03*; Standard Practice for Preparing, Cleaning, and Evaluating Corrosion Test Specimens. ASTM International: West Conshohocken, PA, USA, 2011. [CrossRef]
34. Bazhenov, V.; Koltygin, A.; Komissarov, A.; Anishchenko, A.; Khasenova, R.; Komissarova, J.; Bautin, V.; Seferyan, A.; Fozilov, B. Microstructure, Mechanical and Corrosion Properties of Biodegradable Mg-Ga-Zn-X (X = Ca, Y, Nd) Alloys. In Proceedings of the 27th Anniversary International Conference on Metallurgy and Materials, Brno, Czech Republic, 23–25 May 2018; TANGER Ltd.: Ostrava, Czech Republic, 2018; pp. 1375–1380.
35. Kirkland, N.T.; Birbilis, N.; Staiger, M.P. Assessing the corrosion of biodegradable magnesium implants: A critical review of current methodologies and their limitations. *Acta Biomater.* **2012**, *8*, 925–936. [CrossRef] [PubMed]
36. Tong, L.B.; Zheng, M.Y.; Cheng, L.R.; Zhang, D.P.; Kamado, S.; Meng, J.; Zhang, H.J. Influence of deformation rate on microstructure, texture and mechanical properties of indirect-extruded Mg–Zn–Ca alloy. *Mater. Charact.* **2015**, *104*, 66–72. [CrossRef]
37. Jiang, M.G.; Xu, C.; Nakata, T.; Yan, H.; Chen, R.S.; Kamado, S. Development of dilute Mg–Zn–Ca–Mn alloy with high performance via extrusion. *J. Alloys Compd.* **2016**, *668*, 13–21. [CrossRef]
38. Li, C.; Sun, H.; Li, X.; Zhang, J.; Fang, W.; Tan, Z. Microstructure, texture and mechanical properties of Mg-3.0Zn-0.2Ca alloys fabricated by extrusion at various temperatures. *J. Alloys Compd.* **2015**, *652*, 122–131. [CrossRef]
39. Yu, H.; Tieu, A.K.; Lu, C.; Godbole, A. Investigation of closure of internal cracks during rolling by FE model considering crack surface roughness. *Int. J. Adv. Manuf. Technol.* **2014**, *75*, 1633–1640. [CrossRef]
40. Krbaťa, M.; Eckert, M.; Križan, D.; Barényi, I.; Mikušová, I. Hot Deformation Process Analysis and Modelling of X153CrMoV12 Steel. *Metals* **2019**, *9*, 1125. [CrossRef]
41. Eckert, M.; Krbaťa, M.; Kohutiar, M.; Kuba, M. Hot Deformation Analysis of 100MnCrW4 Tool Steel. *Procedia Struct. Integr.* **2023**, *43*, 318–323. [CrossRef]
42. Kraus, T.; Fischerauer, S.F.; Hänzi, A.C.; Uggowitzer, P.J.; Löffler, J.F.; Weinberg, A.M. Magnesium alloys for temporary implants in osteosynthesis: In vivo studies of their degradation and interaction with bone. *Acta Biomater.* **2012**, *8*, 1230–1238. [CrossRef]
43. Bahmani, A.; Arthanari, S.; Shin, K.S. Formulation of corrosion rate of magnesium alloys using microstructural parameters. *J. Magnes. Alloys* **2020**, *8*, 134–149. [CrossRef]
44. Aung, N.N.; Zhou, W. Effect of grain size and twins on corrosion behaviour of AZ31B magnesium alloy. *Corros. Sci.* **2010**, *52*, 589–594. [CrossRef]
45. Feliu, S. Electrochemical Impedance Spectroscopy for the Measurement of the Corrosion Rate of Magnesium Alloys: Brief Review and Challenges. *Metals* **2020**, *10*, 775. [CrossRef]
46. Randviir, E.P.; Banks, C.E. Electrochemical Impedance Spectroscopy: An Overview of Bioanalytical Applications. *Anal. Methods* **2013**, *5*, 1098–1115. [CrossRef]
47. Feliu, S.; Galvan, J.K. The application of electrochemical impedance spectroscopy to study the corrosion of magnesium alloys. In *Encyclopedia of Solid-Liquid Interfaces*, 1st ed.; Wandelt, K., Bussetti, G., Eds.; Elsevier: Amsterdam, The Netherlands, 2024; pp. 550–564. [CrossRef]
48. Nakatsugawa, I.; Martin, R.; Knystautas, E.J. Improving Corrosion Resistance of AZ91D Magnesium Alloy by Nitrogen Ion Implantation. *Corrosion* **1996**, *52*, 921–926. [CrossRef]
49. Sun, M.; Yerokhin, A.; Bychkova, M.Y.; Shtansky, D.V.; Levashov, E.A.; Matthews, A. Self-Healing Plasma Electrolytic Oxidation Coatings Doped With Benzotriazole Loaded Halloysite Nanotubes on AM50 Magnesium Alloy. *Corros. Sci.* **2016**, *111*, 753–769. [CrossRef]

50. Coy, A.E.; Viejo, F.; García-García, F.J.; Liu, Z.; Skeldon, P.; Thompson, G.E. Effect of Excimer Laser Surface Melting on the Microstructure and Corrosion Performance of the Die Cast AZ91 Magnesium Alloy. *Corros. Sci.* **2010**, *52*, 387–397. [CrossRef]
51. Liu, H.; Cao, F.; Song, G.L.; Zheng, D.; Shi, Z.; Dargusch, M.S.; Atrens, A. Review of the Atmospheric Corrosion of Magnesium Alloys. *J. Mat. Sci. Technol.* **2019**, *35*, 2003–2016. [CrossRef]